Chemical Engineering Journal 519 (2025) 165467

Contents lists available at ScienceDirect

Chemical Engineering Journal

journal homepage: www.elsevier.com/locate/cej

Synthesis of beta-supported Cr/Sn bimetallic nanoparticles via ultrafast thermal shock for high yield of lactic acid

Mengyu Jin [a], Yuanbo Song [a], Shijie Wang [a], Cheng Hou [b], Xiaoxia Wang [a], Yang Shi [a], Zheng Shen [a,c,*], Yalei Zhang [b,c]

[a] *Institute of New Rural Development, School of Electronics and Information Engineering, Tongji University, Shanghai 201804, China*
[b] *State Key Laboratory of Pollution Control and Resources Reuse, College of Environmental Science and Engineering, Tongji University, Shanghai 200092, PR China*
[c] *Key Laboratory of Rural Toilet and Sewage Treatment Technology, Ministry of Agriculture and Rural Affairs, Shanghai 201804, China*

ARTICLE INFO

Keywords:
Ultrafast thermal shock
Bimetallic nanomaterials
Size effect
Selective catalysis
Lactic acid

ABSTRACT

The size dependence of metal nanoparticles is a critical factor affecting catalytic activity, as their geometric and electronic properties vary significantly with size. This study proposes a strategy combining rapid Joule-heating with solid-phase synthesis to prepare Cr/Sn-Beta bimetallic catalysts of various sizes via ultrafast thermal shock (UTS, heating rate: 1850 °C/s) and conventional muffle furnace annealing (MFA, heating rate: 5 °C/min). HRTEM results reveal that the bimetallic particle size of Cr/Sn-Beta catalysts prepared via UTS technique is only 2.55 nm, compared to 6.54 nm for catalysts obtained through conventional MFA method. Combined with XRD, BET, H_2-TPR, UV–vis and FT-IR characterization, it is further confirmed that the ultra-high heating/cooling rate and second-short heating duration of the UTS method achieved efficient embedding of Cr and Sn within the zeolite micropores, which conferred precise tailoring of the particle size. The correlation between particle size and catalytic activity was investigated using the LA production from cellulose as a model reaction. In this work, the superior size effect of bimetallics nanoparticles prepared by UTS synthesis strategies was emphasized, providing insights into the geometry-activity relationship that will guide the rational design of catalysts in terms of morphology and particle size.

1. Introduction

Given the finite availability of fossil resources and the environmental issues arising from their widespread utilization, the need to prepare green degradable materials from biomass has become increasingly urgent [1,2]. With the increasing popularity of degradable plastics, polylactic acid materials are attracting much attention, thus making lactic acid (LA) one of the most promising renewable monomers among the many biomass-based products [3]. Consequently, the development of cost-effective strategies for LA synthesis holds significant importance in advancing the field of green chemistry [4,5]. Due to the limited sustainability of conventional biofermentation methods, exploring innovative chemocatalytic methods for the direct synthesis of LA from lignocellulosic biomass is essential [6]. Owing to their unique characteristics, such as size effects, nanoparticles find broad application in catalysis and energy conversion [7]. Metal nanoparticles are frequently stabilized on porous carbon or oxide supports during catalyst synthesis to avoid aggregation. The efficiency of the catalyst is strongly influenced by the particle size and loading level, as smaller particles and higher loadings generally boost the number of active sites, thereby greatly improving catalytic performance [8]. However, the synthesis and assembly of nanoparticles remain challenging, particularly for highly reactive materials such as non-precious metals, where the size of the metal nanoparticles plays a critical role in metal-catalyzed heterogeneous reactions [9]. Therefore, there is a growing need for a fast, cost-effective, and scalable approach to producing uniformly distributed nanoparticles, especially for energy applications.

In addition, bimetallic catalysts exhibit excellent catalytic reaction performance compared to monometallic component catalysts due to the synergistic coupling between the constituent elements that can connect the catalytically active sites [10–12]. Consequently, researchers have increasingly focused on bimetallic catalysts composed of two metal elements, motivated by their potential to improve catalytic efficiency and structural stability through synergistic interactions between the metals [13–16]. However, the broad reduction potentials and uncontrollable nucleation dynamics between different metal elements have posed

---

* Corresponding author at: Institute of New Rural Development, School of Electronics and Information Engineering, Tongji University, Shanghai 201804, China.
E-mail address: shenzheng@tongji.edu.cn (Z. Shen).

https://doi.org/10.1016/j.cej.2025.165467
Received 25 February 2025; Received in revised form 5 June 2025; Accepted 28 June 2025

significant challenges to the synthesis of bimetallic nanoparticles [17,18]. Moreover, the thermodynamic instability and the inherent tendency of particles to aggregate further exacerbate the challenges in achieving precise size control of bimetallic nanoparticles [19,20]. Investigating the nature of active sites at the atomic and molecular levels is highly challenging due to the structural complexity of bimetallic catalysts, which includes factors such as particle dispersion and homogeneity [21,22]. Against this backdrop, the rational selection of synthesis methods and precisely control the structure and composition are essential for the development of efficient and stable bimetallic catalysts. To enhance the stability of bimetallic particles, it is often necessary to strengthen the interaction between the metal and its support. This can be achieved through an appropriate heat treatment, such as increasing the temperature to provide the required activation energy for creating atomically dispersed catalysts [18]. Meanwhile, another issue associated with uniformly distributed nanoparticles is the aggregation caused by thermodynamic processes, emphasizing the importance of rapid heating and cooling rates [23]. However, conventional methods, such as muffle furnace annealing (MFA), are limited in controlling nanoparticle size, leading to metal coarsening and size inconsistency, which hinder the fabrication of ultrafine, uniformly distributed bimetallic nanoparticles [24–26].

Recently, flash Joule-heating technology has emerged as an efficient and versatile method for transient nanoparticle synthesis, offering precise thermal control and rapid processing (in seconds) [27,28]. The principle involves using DC discharge and instantaneous high temperatures to rapidly decompose polymetallic precursors into nanoparticles, preventing the aggregation typically induced by prolonged high-temperature annealing in conventional thermal processes. In 2016, the research group led by Professors Ya-Nan Chen and Liang-Bing Hu first introduced the high-temperature thermal shock technique and applied it to the rapid synthesis of nanomaterials. This method enables the in-situ synthesis of uniformly dispersed nanoparticles on carbon substrates through thermal shock treatment [29]. In particular, the intense heat from thermal shock breaks down metal salt precursors into metal clusters, which quickly form evenly distributed nanoparticles on the carbon support during the rapid cooling phase, all within milliseconds. The team has successfully created a diverse array of functional nanomaterials, such as metal alloys, carbon-based compounds, and semiconductors [27,30–32]. Hou et al. successfully developed an efficient electrocatalyst Ru/Mo_2N, and achieved a uniform dispersion of Ru on Mo_2N by using a rapid heating method. Experimental analyses showed that Ru exhibited a higher degree of electron transfer during high-temperature shock and a synergistic effect between Ru sub-nanoparticle sites and Mo_2N, which promoted abundant metal-carrier interactions that conferred the excellent performance of Ru/Mo_2N [33]. Shi et al. reported a universal and efficient method for synthesizing ultra-small, high-density nanoparticles by directly pyrolyzing metal-ligand precursors through carbon thermal shock (~100 ms), eliminating the need for time-consuming metal-organic framework (MOF) preparation. This method facilitated the creation and stabilization of high-density nanoparticles on two-dimensional porous carbon membranes [34]. A comparison with other emerging rapid or energy-efficient synthesis methods, including flame spray pyrolysis (FSP), microwave-assisted heating, and conventional muffle furnace annealing (MFA), is summarized in Table S1. Among these, ultrafast thermal shock (UTS) uniquely achieves ultrafast heating (>1000 °C/s) and precise particle size control within seconds, enabling efficient embedding of metal nanoparticles into zeolite micropores without agglomeration or structural collapse, which is often challenging for FSP or microwave-based routes. Recognizing the significant potential of UTS method for electrocatalysis, the use of various experimental parameters (such as precursor concentration, precursor/metal ratio, reaction time/temperature/heat shock cycles) to control the nucleation and growth of metal particles makes its application in biomass catalysis highly promising. However, the relationship between nanoscale modulation of bimetallic catalysts and LA production from biomass still requires further investigation.

In this paper, we successfully loaded bimetallic nanoparticles smaller than 3 nm in situ on Beta molecular sieve carriers using a high temperature UTS strategy based on flash Joule heating. Due to the rapid heating/cooling process in seconds to limit the migration of metal atoms, which inhibits the aggregation of nanoparticles and improves the dispersion of active sites, the metal species were more accessible to the backbones and confined in the interior of the micropores. The Cr-Sn bimetallic acted in different cascade reaction steps, which improves the lactic acid yield of the whole reaction system. This research explores the size dependence of nanoparticles in catalysis, contributing to a deeper understanding of the structure-activity relationship in heterogeneous bimetallic catalysts.

2. Materials and methods

2.1. Materials

Cellulose obtained from pre-treated corn straw were purchased from Taobao, and then crushed and pretreated with a crusher, finally sieved to pass through a 40-mesh sieve and retained by a 60-mesh sieve. Tin (II) acetate was purchased from Sigma-Aldrich. Chromic acetate (99.9%), stannic oxide (AR, 99.5%), chromium sesquioxide (AR, 99.0%), formic acid (≥98%), acetic acid (99.8%), glycolic acid (98%) were obtained from Aladdin. Lactic acid (1.0 M) was purchased from Alfa Aesar. 5-Hydroxymethylfurfural (>99%) was purchased from Macklin. The commercial Beta zeolite (Si/Al ratio of 25) was purchased from Tianjin Nanhua Catalyst Co., Ltd. (Tianjin, China).

2.2. Synthesis of beta-supported Cr/Sn bimetallic nanoparticles

All catalysts were synthesized by a solid-state ion exchange method. A stoichiometric mixture of chromium and tin acetates (Cr/Sn = 3:5 molar ratio) was thoroughly ground with 1 g of deAl-Beta zeolite in an agate mortar for 30 min to ensure homogeneous mixing. The resulting powder was then subjected to UTS or conventional MFA calcination.

Preparation of deAl-Beta: Firstly, the Beta zeolite (12.5 g) were placed in a round-bottomed flask containing 250 mL of concentrated nitric acid (65% concentration), and then the flask was placed in an oil bath at a controlled temperature of 100 °C with stirring at a rate of 200 rpm to dealuminate the Beta zeolite for 22 h. The dealuminated mixture was separated by centrifugation in a high-speed centrifuge (8000 rpm for 5 min), and then the solid material was washed with deionized water until the solution was pH neutral. The washed solid material was dried in an oven at 70 °C and then transferred to 150 °C for further drying overnight to obtain the dealuminated Beta zeolite, which was denoted as deAl-Beta.

Preparation of the catalyst by MFA method: The procedure for the preparation of Cr/Sn-Beta-MFL catalysts by muffle furnace annealing is as follows: a certain amount of metal acetate was mixed with 1 g deAl-Beta and then milled in an agate mortar for 30 min; the milled samples were roasted by a programmed temperature increase in a muffle furnace at 550 °C for 6 h. Finally, the catalysts were denoted as Cr/Sn-Beta-MFA.

Preparation of the catalyst by UTS method: The procedure for the preparation of Cr/Sn-Beta-UTS catalysts by ultrafast thermal shock is as follows: a certain amount of metal acetate was mixed with 1 g deAl-Beta and then milled in an agate mortar for 30 min; the milled samples were heated to high temperature shock by a Joule heating device purchased from Hefei In-situ Technology Co., Ltd. The synthesizer is equipped with a DC power supply, with a maximum output voltage of 40 V. Using a carbon rod as the conductive substrate, a direct current (DC) power supply controls the current flow through the carbon rod to generate Joule heat. The carbon rod is fixed at both ends with screws to ensure current continuity. The precursor powder is filled into the carbon rod, and Joule heating is applied by adjusting different voltages (10–30 V) and currents (10–30 A). The heating temperature can reach 600 °C to 1100 °C in approximately 3 s. Finally, the catalysts were denoted as Cr/Sn-Beta-UTS.

2.3. *Characterization*

The morphology and microstructure of the catalysts were characterized using transmission electron microscopy (TEM, FEI Talos F200X G2). The diffraction pattern was obtained using an X-ray diffractometer (XRD, TDM-20) equipped with a 9 KW Cu Kα radiation source (λ = 0.15418 nm). Specific surface area, pore size distribution and total pore size and micropores were analyzed volumetrically by nitrogen adsorption-desorption experiments using a Micromeritics ASAP 2460. The content of metals (i.e. Sn and Cr) in the synthesis catalysts was determined by ICP-OES (Agilent 5110). X-ray photoelectron spectroscopy (XPS, Thermo Scientific ESCALAB 250Xi) was employed to determine the surface valence state of the catalyst. The binding energies of all elements were calibrated using the C 1s peak at 284.8 eV. Fourier transform infrared spectroscopy (FTIR, Thermo Fisher Scientific Nicolet iS20) and diffuse reflectance ultraviolet visible spectrum (UV–vis, Shimadzu UV-3600) were applied to investigate the structural properties of the catalysts. Pyridine infrared (Py-IR, Bruker Tensor 27) spectra were analyzed in the 1400 to 1700 cm^{-1} region to explore the type of acid on acidic solid catalysts surfaces. H_2-temperature-programmed reduction (TPR, BSD-Chem C200) was used to analyze the reactive metal species. XAFS spectra were recorded at the Cr and Sn K-edges and analyzed using Athena and Artemis software. EXAFS data were fitted in both K- and R-space using Cr and Sn foil as standards. Additionally, wavelet transform (WT) analysis was performed using the Morlet function ($\kappa = 10$, $\sigma = 1$) to differentiate metal–oxygen (M—O) and metal–metal (M—M) coordination shells in the joint K–R space.

2.4. *Reaction tests and product analysis*

The catalytic reactions were carried out in a batch-type hydrothermal reactor with a volume of 50 mL. The reactor was fixed on the rotating shaft of the rotating oven to carry out the reaction. Firstly, 150 mg substrate, 150 mg catalyst and 10 mL water were added to the reactor liner. The reaction mixture was then placed in a rotary oven at a controlled temperature of 270 °C for 3 h at a rotational speed of 200 rpm. The reaction was quenched by placing the reactor in cold water immediately after the reaction. The measurements were repeated for each set of experiments to determine the reproducibility of the data. The liquid and solid products were collected separately by centrifugation and the liquid products were analyzed by HPLC after passing through a 0.22 μm membrane. The liquid phase products were analyzed using a UV detector of Primaide HPLC equipped with an Aminex HPX-87H column, operating at a column temperature of 35 °C. The mobile phase consisted of 5 mM H_2SO_4, and the flow rate was set at 0.5 mL min^{-1}. The total organic carbon (TOC) measurement was conducted using an Jena Multi N/C 3100 analyzer. The product yields and carbon balance analysis method are provided in the Supporting Information (Text S1, Text S2). The molecular configurations in each system were equilibrated using the Compass force field in the Materials Studio 2020 software. The deAl-Beta Zeolite structures were obtained from the International Zeolite Association (IZA) database. The energy cut-off was then set to 600 eV in the CASTEP module, and all density-functional theory calculations were completed using the norm-conserving pseudopotential and the Generalized-Gradient-Approximation (GGA) Perdew-Burke-Ernzerhof (PBE). The calculation method of adsorption energy is detailed in supporting information Text S3.

3. Results and discussion

3.1. *Schematic comparison of UTS method and traditional MFA method*

In this study, we synthesized Cr/Sn-Beta catalysts using the same precursors for comparison, employing both the rapid thermal shock strategy and the conventional furnace calcination method (Fig. 1a). Firstly, Beta zeolite were treated with concentrated nitric acid to remove Al atoms from the framework, yielding deAl-Beta. Subsequently, the deAl-Beta was milled with a specific ratio of bimetallic Cr-Sn metal salts to produce metal salt-loaded deAl-Beta precursors. Finally, the precursors were processed using both muffle furnace calcination and rapid thermal shock using Joule heating denoted as Cr/Sn-Beta-MFA and Cr/Sn-Beta-UTS, respectively. The UTS strategy shows unique advantages over the conventional furnace annealing method, which can provide considerably higher energy densities and faster heating/cooling rates, simple synthesis process/lower energy consumption and smaller nanoparticle sizes/morphologies (Fig. 1b). This synthesis strategy has four main advantages: 1) In contrast, during conventional MFA treatment, the inherently slow heating/cooling rate (~5 °C/min) and prolonged heating duration (6 h) (Fig. 1c) make it challenging to achieve precise control over the organization of metal nanoparticles, leading to undesirable effects such as coarsening, growth, agglomeration, uneven size distribution, and volatilization of constituent metals. The UTS method limits the migration of metal atoms due to the ultra-high heating/cooling rate (~1850 °C/s) and short heating duration (2 s) (Fig. 1d), which inhibits the aggregation of nanoparticles and improves the dispersion of active sites. 2) Solid-state ion exchange ensures uniform precursor mixing, enabling high Cr-Sn loading and even distribution. 3) Anchoring ligand-free Cr-Sn nanoparticles on deAl-Beta with abundant vacancies prevents aggregation. 4) The catalytic performance can be tailored by adjusting heating temperature (Fig. 1e), duration (Fig. 1f), and thermal shock cycles (Fig. 1g). To confirm reproducibility, five batches of Cr/Sn-Beta-UTS catalysts were prepared under identical UTS conditions (Table S2). ICP-OES results showed consistent Cr (0.91–1.02 wt%) and Sn (1.86–2.01 wt%) loadings across batches. Catalytic activity tests also showed stable LA yields (49.37–54.27%) under the same conditions, verifying the batch consistency of the UTS method.

3.2. *Structure characterization*

To compare the physicochemical properties and morphology of the catalysts, nitrogen adsorption-desorption analyses were performed on Beta, deAl-Beta, and various metal-loaded catalysts. Table S3 summarizes the physical properties, including metal content, specific surface area, and pore characteristics. Fig. 2a presents the N_2 adsorption-desorption isotherms, which, according to IUPAC classification, exhibit Type IV isotherms and H1 hysteresis loops, indicating the formation of a small fraction of mesoporous structures [35]. The Beta zeolite exhibited a specific surface area (S_{BET}) of 611.8 m^2/g and a total pore volume of 0.37 cm^3/g. Following HNO_3 dealumination, S_{BET} decreased to 541.8 m^2/g (deAl-Beta), while the total pore volume increased to 0.99 cm^3/g. Upon introducing Cr and Sn, S_{BET} of Cr/Sn-Beta-MFA and Cr/Sn-Beta-UTS catalysts were reduced to 490.47 m^2/g and 488.35 m^2/g, respectively, with total pore volumes of 0.39 cm^3/g and 0.35 cm^3/g. This decrease suggests uniform dispersion of Cr and Sn within the zeolite pores [36]. Notably, the Cr/Sn-Beta-UTS catalyst displayed smaller surface area, pore volume, and pore size compared to Cr/Sn-Beta-MFA, potentially due to greater incorporation of metals into the zeolite framework or micropores during UTS synthesis.

As shown in Fig. 2b, XRD was used to characterize the crystal structures of the samples. All XRD patterns displayed the typical BEA topology, and the crystallinity of Beta zeolite was maintained after dealumination and metal loading, indicating that these processes do not disrupt the zeolite structure [37]. On the other hand, the deAl-Beta zeolite generates a large number of structural vacancies, providing

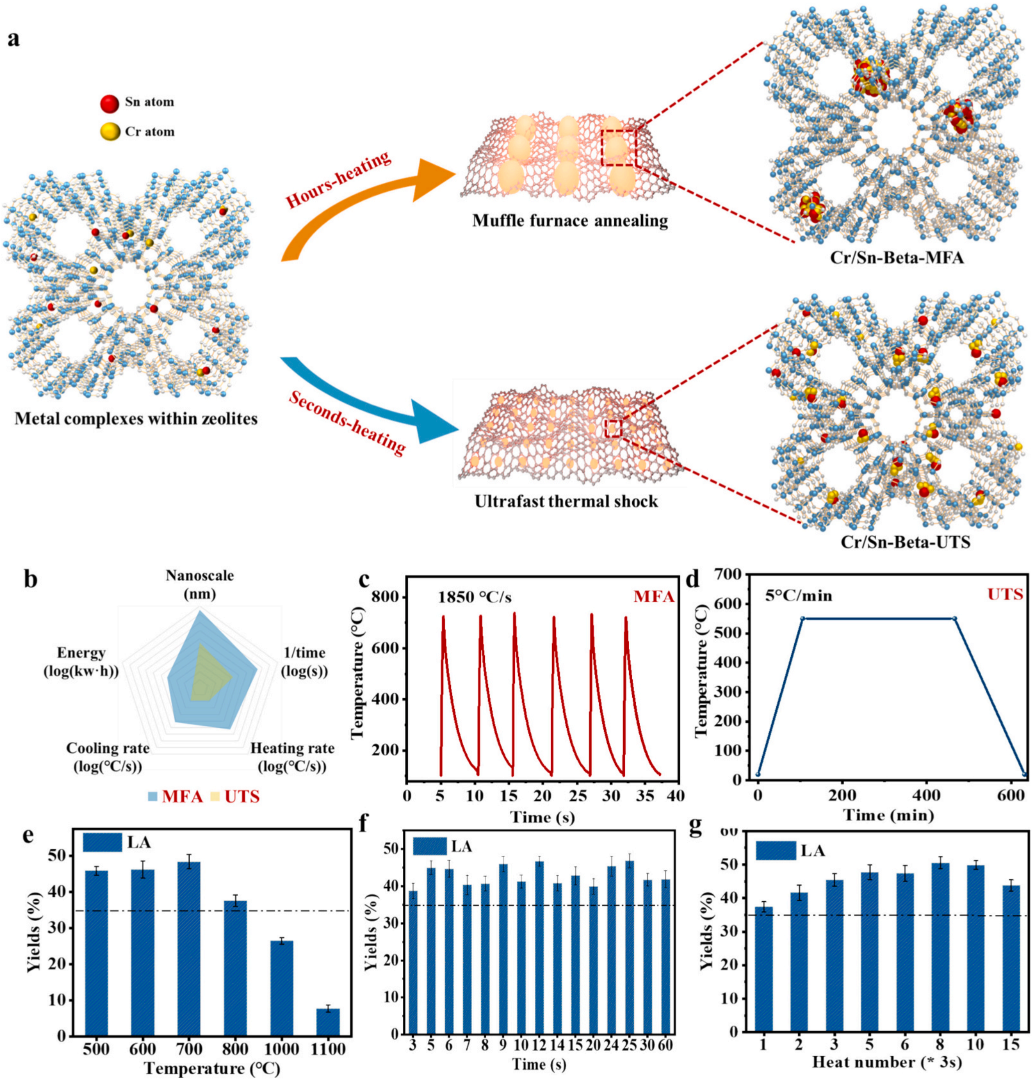

Fig. 1. (a) Scheme illustrating the synthesis process for Cr/Sn-Beta-MFA and Cr/Sn-Beta-UTS. (b) A radar plot showing a comparison between the conventional MFA method and our UTS approach, evaluating reaction duration, heating/cooling rates, energy, and nanoscale uniformity. The reaction duration is presented as the inverse of time, with the higher value from the two methods normalized to 1. (c, d) Temperature profiles of the MFA and UTS processes. The whole MFA and UTS process takes ≈10 h and ≈38 s, respectively. (e) Thermal shock treatment at different temperatures. (f) Thermal shock treatment at different time. (g) Thermal shock treatment at different heat numbers.

ample sites for metal integration. After dealumination, the 2θ value of the main diffraction peak shifted from 22.72° (Beta) to 22.76° (deAl-Beta), indicating successful removal of Al atoms and a contraction of the Beta framework, consistent with previous studies (Fig. 2c) [38]. Meanwhile, it is worth noting that after metal loading by different methods, the main diffraction peaks shifted to lower angles, indicating an increase in zeolite lattice spacing due to the incorporation of Cr and Sn into the framework. The shift was more pronounced for the Cr/Sn-Beta-UTS catalyst, which exhibited a 0.2° shift compared to the 0.04° shift observed for Cr/Sn-Beta-MFA. The lattice spacing expanded from 3.9045 Å ($2\theta = 22.799°$) to 3.9377 Å ($2\theta = 22.592°$), suggesting that most of the metals successfully integrated into the zeolite framework or micropores, leading to lattice distortion [39]. However, the crystal face spacing of 3.9168 Å ($2\theta = 22.685°$) for the MFA method did not change significantly, suggesting that the metal did not enter the molecular sieve skeleton and was more loaded on the outer surface of the carrier. It is further confirmed that the UTS method Cr and Sn atoms are more into the zeolite backbone for coordination and formation of domain-limited metals within the zeolite microporous pores. The morphology and size of the synthesized Cr-Sn bimetallic nanoparticles were analyzed using high-resolution transmission electron microscopy (HRTEM) images, while EDX spectra verified the uniform distribution of silicon, oxygen, and the respective metal elements (Fig. 2d, e). To validate the nanoscale bimetallic structure, high-resolution XEDS mapping images of Cr/Sn-Beta catalysts prepared by both MFA and UTS methods (Cr/Sn = 3:5) were acquired and shown in Fig. S1. The spatial overlap between Cr and Sn signals confirms the formation of bimetallic nanoparticles. XEDS quantification analysis on selected nanoparticle regions (Figs. S2, S3; Tables S4, S5) further confirmed that both Cr and Sn were successfully incorporated, with a slight enrichment of Sn likely due to surface segregation or precursor dynamics during ultrafast heating.

The Cr/Sn-Beta catalyst prepared by conventional muffle furnace calcination exhibited bimetallic particle sizes of approximately 6.54 nm, which are attributed to aggregation on the zeolite surface. In contrast, the Cr/Sn-Beta-UTS catalyst had metal particle sizes of around 2.55 nm, demonstrating smaller particles and better dispersion. These results are consistent with the nitrogen adsorption-desorption and XRD data. Generally, the UTS method is an effective means of rapidly achieving ultra-high temperatures. The UTS generated in seconds facilitates the bonding of the target metals with the support. During Cr and Sn loading

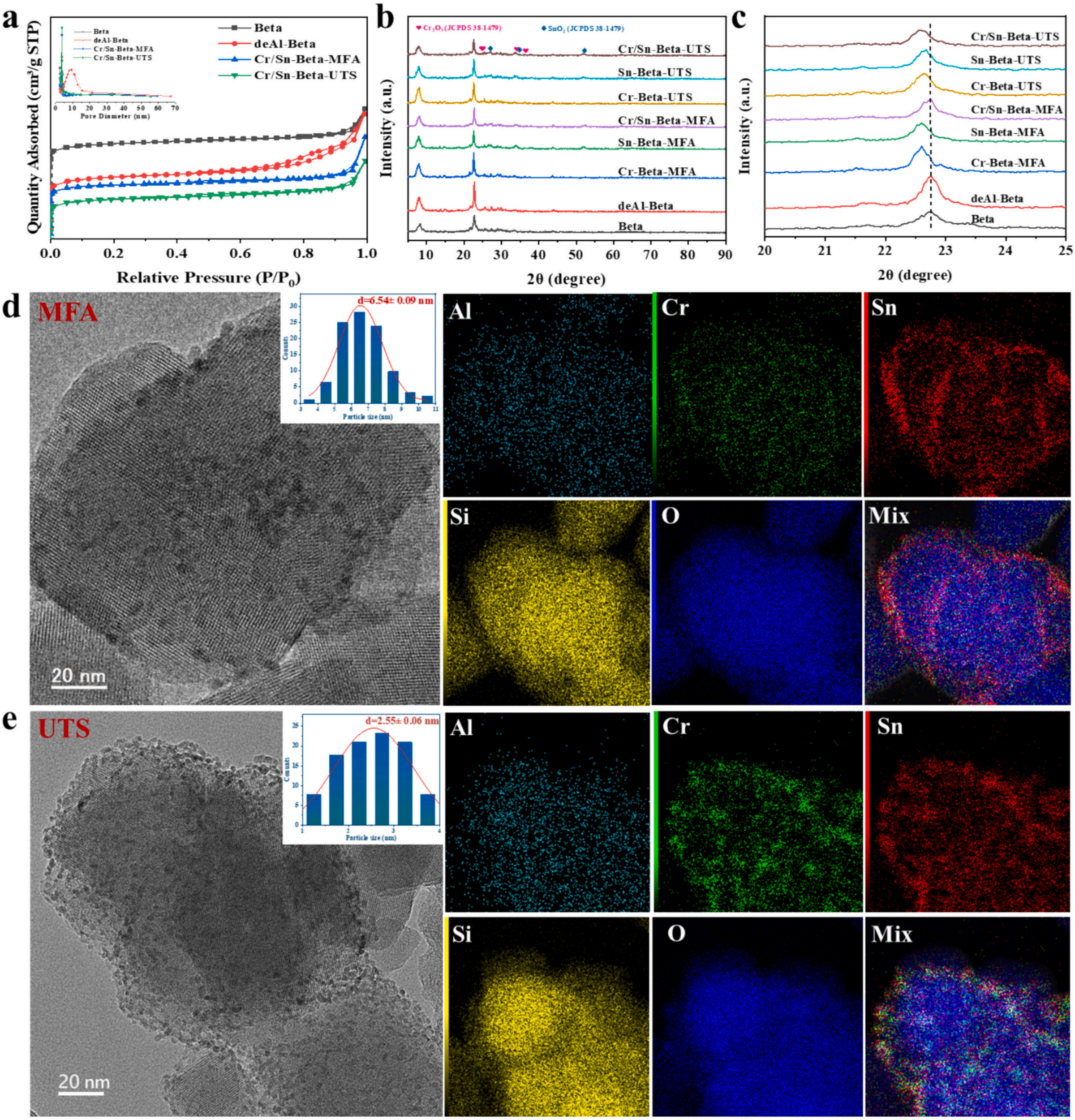

Fig. 2. (a) N_2 absorption-desorption isotherms (inset pore distribution) of different samples. (b) XRD patterns and (c) XRD magnified images of different samples. (d, e) HRTEM images (inset particle size distribution), and EDX-elemental mapping images of Cr/Sn-Beta-MFA and Cr/Sn-Beta-UTS.

onto the zeolite, the localized high temperature from Joule heating promotes rapid decomposition and interaction of the metal precursors, resulting in the formation of ultra-fine bimetallic nanoparticles. This process enhances the diffusion of the metal species into the micropores of Beta zeolite, promoting metal entry and reducing particle size due to confinement effects. In contrast, the MFA method leads to partial deposition of metal species on the zeolite external surface or pore openings, resulting in larger particles and greater aggregation. In conclusion, the UTS method produces smaller bimetallic nanoparticles that are more effectively incorporated into the molecular sieve framework.

3.3. Identification of chemical state and electronic properties

UV–vis spectra were used to characterize the metal species and coordination states of the heteroatom-loaded zeolites. As shown in Fig. 3a, distinct absorption peaks for Sn species appear near 200 and 225 nm in the Sn-Beta-MFA/UTS and Cr/Sn-Beta-MFA/UTS catalysts. These observations are consistent with previous reports and strongly confirm the successful synthesis of BEA topology zeolite materials enriched with tetrahedrally coordinated Sn in the framework [40,41]. Furthermore, the catalyst synthesized via the UTS method shows a stronger absorbance intensity compared to the MFA method, indicating a higher

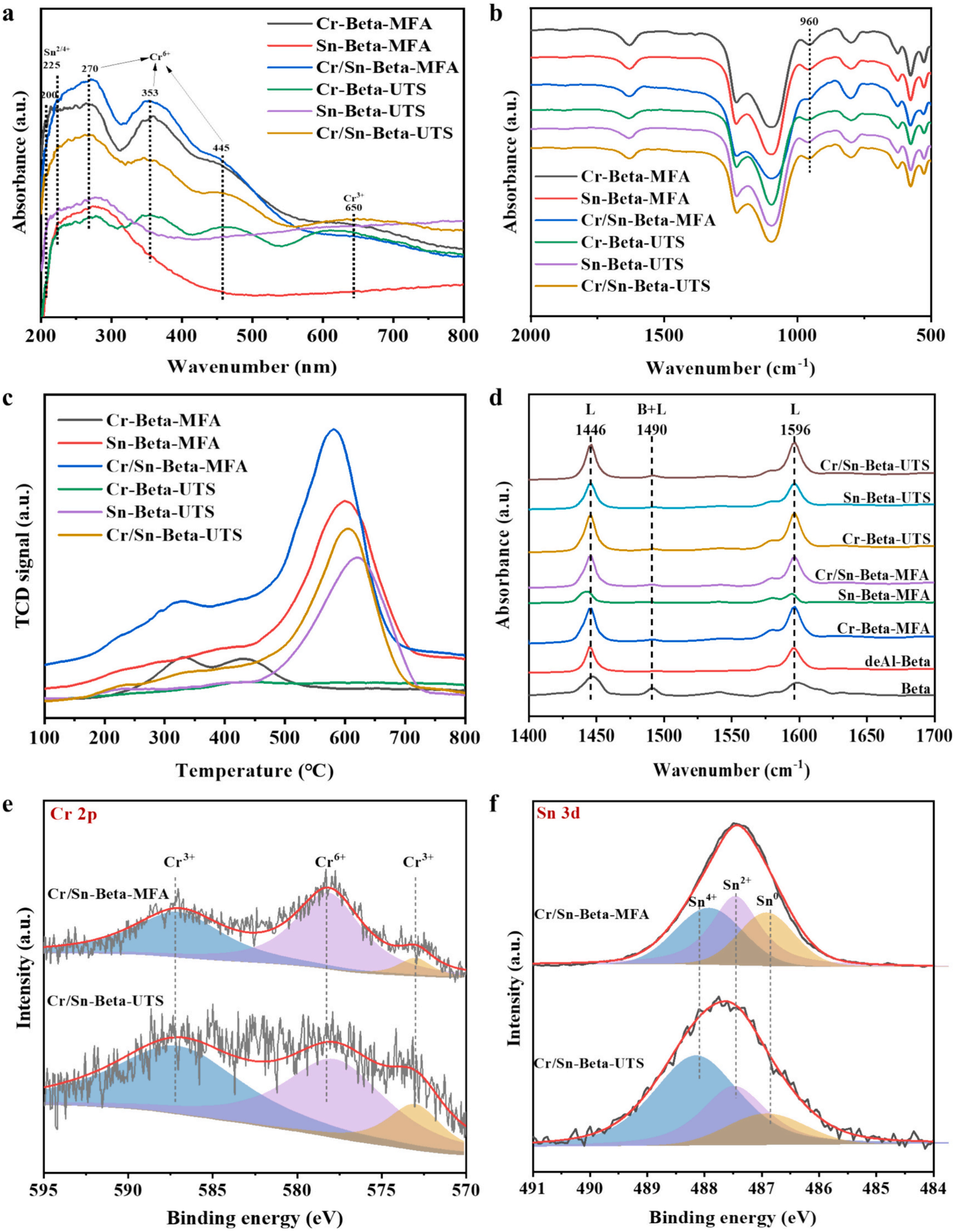

Fig. 3. (a) UV–vis spectra (b) FT-IR spectra (c) H_2-TPR (d) Py-IR spectra (e) XPS spectra of Cr 2p (f) XPS spectra of Sn 3d of different samples.

content of framework Sn. UV–vis spectra also show Cr species oxidation states, with peaks at 270 nm, 353 nm, and 445 nm corresponding to Cr (VI) species, and a peak around 650 nm indicative of Cr(III) d-d transitions [42]. Cr(VI) and Cr(III) species coexist in Cr/Sn-Beta-MFA/UTS, but Cr(III) species dominate in Cr/Sn-Beta-UTS. In M-Beta, the catalytic active sites are attributed to the M—O—Si bonds within the framework. The absorption peak at 960 cm^{-1} in the FT-IR spectra is commonly associated with the substitution of framework Al atoms by other metal heteroatoms. Fig. 3b presents the FT-IR spectra of catalysts synthesized via different methods. Notably, all samples display an absorption peak at 960 cm^{-1}, which provides clear evidence of metal incorporation into the zeolite framework [43]. Fig. 3c shows the H_2-TPR profiles of Cr/Sn-Beta-MFA and Cr/Sn-Beta-UTS catalysts. For the Cr-Beta-MFA catalyst, two distinct reduction peaks are observed at 330 °C and 430 °C, corresponding to the reduction of Cr^{6+} and Cr^{3+} species, respectively. In the case of Cr/Sn-Beta-MFA, the reduction peak at 435 °C is largely diminished, indicating a lower Cr^{3+} content and the predominance of aggregated Cr^{6+} species on the zeolite surface. In contrast, Cr-Beta-UTS and Cr/Sn-Beta-UTS catalysts exhibit no distinct Cr species reduction peaks, suggesting that Cr is predominantly incorporated into the micropores of the zeolite. This strong confinement effect fosters robust interactions between the zeolite framework and Cr species, rendering them difficult to reduce. For Sn-Beta-MFA/UTS and Cr/Sn-Beta-MFA/UTS catalysts, reduction peaks observed at 220 °C and

582 °C are attributed to the reduction of Sn species. Notably, compared to Sn-Beta-MFA and Cr/Sn-Beta-MFA, the high-temperature reduction peaks for Sn-Beta-UTS and Cr/Sn-Beta-UTS shift to higher temperatures. This indicates that the ultrafast high-temperature sintering in the UTS method enhances particle integration, resulting in stronger mechanical and interfacial bonding between Sn species and the zeolite support. Overall, these results demonstrate that the UTS method enables Cr and Sn species to be more effectively incorporated into the zeolite framework and partially confined within the micropores, leading to higher dispersion and stabilization of the metal species.

The type, quantity, and strength of acidic sites play a decisive role in catalytic LA production from cellulose. As shown in the Py-IR results (Fig. 3d, Table S6), dealumination effectively removed Brønsted acid sites, while Lewis acid sites were regenerated upon metal incorporation. The transition metal Cr introduces more Lewis acid sites compared to metal Sn. Catalysts synthesized via the UTS method consistently exhibit higher Lewis acid site density than those prepared by MFA, suggesting that UTS effectively reduces nanoparticle size and optimizes acid site distribution. Furthermore, the effective coupling of the two metals underscores the importance of a well-balanced acid site distribution for achieving superior catalytic performance. NH_3-TPD analysis (Fig. S4, Table S6) further reveals that Cr/Sn-Beta-UTS possesses the highest total acidity and a greater proportion of strong acid sites compared to MFA-treated samples, supporting its superior catalytic performance.

The surface oxidation states of metals in the catalyst significantly influence its catalytic performance. XPS analysis was conducted to study the chemical states of Cr and Sn species in Cr/Sn-Beta-MFA and Cr/Sn-Beta-UTS catalysts, with the calculated elemental contents summarized in Table S7. The Cr 2p XPS spectra (Fig. 3e) reveal three peaks at approximately 587.2 eV, 578.3 eV, and 573.0 eV. The binding energies at 587.2 eV and 573.0 eV correspond to Cr^{3+} species, while the peak at 578.3 eV is attributed to Cr^{6+} [44]. The Cr^{3+} content in the Cr/Sn-Beta-UTS catalyst was 58.59%, compared to 48.17% in Cr/Sn-Beta-MFA, indicating that the UTS method favors the formation of Cr^{3+} species, while the muffle furnace calcination method predominantly produces Cr^{6+}. This observation aligns with the H_2-TPR results. For Sn species (Fig. 3f), three types were identified in both Cr/Sn-Beta-MFA and Cr/Sn-Beta-UTS catalysts. The Sn $3d_{5/2}$ XPS peaks at binding energies of 486.8 eV, 487.5 eV, and 488.1 eV are attributed to Sn^0, Sn^{2+}, and Sn^{4+} species, respectively [45]. The Cr/Sn-Beta-UTS catalyst predominantly features Sn^{4+} species (54.98%), whereas the Cr/Sn-Beta-MFA catalyst is dominated by Sn^{2+} species (39.96%). This disparity likely arises from the oxidative conditions during pyrolysis. The UTS method minimizes metal atom migration, allowing Cr atoms to occupy Al vacancies, thereby stabilizing Cr^{3+} and favoring Sn^{4+} formation. In contrast, the MFA method promotes surface aggregation of metal species, leading to oxidation and electron transfer between Cr and Sn, resulting in Cr^{6+} and Sn^{2+} species. Furthermore, Table S7 indicates that the bulk Sn content in Cr/Sn-Beta-UTS is significantly lower than its surface Sn content, confirming that UTS facilitates the incorporation of Sn species into the zeolite framework or micropores.

To investigate the local coordination environments of metal species and elucidate their structure–activity relationships, solid-state ^{29}Si and ^{1}H MAS NMR, X-ray absorption fine structure (XAFS), and wavelet transform (WT) analyses were conducted. As shown in Fig. 4, ^{29}Si MAS NMR spectra revealed two categories of signals: Q^4-type silicon (−110 to −115 ppm) representing $Si(OSi)_4$ units and Q^3-type species (−100 to −105 ppm) related to silanol defects. The UTS-treated sample exhibited a significantly higher fraction of Q^3 sites (17.4%) compared to the MFA-treated counterpart (5.3%), as quantified in Table S8, indicating enhanced framework defects that can act as anchoring sites for metal ions. ^{1}H MAS NMR spectra showed two characteristic signals at 4.18 ppm and 6.27 ppm, corresponding to bridging hydroxyls (Si–OH–M) and ultra-strong Brønsted acid sites, respectively. The Cr/Sn-Beta-UTS catalyst exhibited a higher proportion of bridging hydroxyls (65.7%) than Cr/Sn-Beta-MFA (24.7%), indicating a higher density of acid sites (Table S9) and greater potential for proton transfer and biomass activation.

EXAFS fitting further confirmed that both Cr and Sn were present in highly dispersed states. As shown in Fig. 5a, b, the normalized XANES spectra at the Cr and Sn K-edges revealed oxidation states of Cr^{3+} and Sn^{4+}, consistent with Cr_2O_3 and SnO_2 references. The corresponding radial distribution functions (χ(R), Fig. 5c, d) revealed well-defined Cr—O (1.99 Å, CN ≈ 4.3) and Sn—O (2.04 Å, CN ≈ 6.1) scattering paths, with only minor Cr-Cr and Sn-Sn contributions at 2.95 and 3.18 Å, respectively. These values suggest that the metal species are present as small clusters or are partially incorporated into the zeolite framework, rather than forming large agglomerates. The fitting parameters are summarized in Table S10. To further distinguish overlapping scattering features, wavelet transform (WT) was applied (Fig. 5e, f). The WT

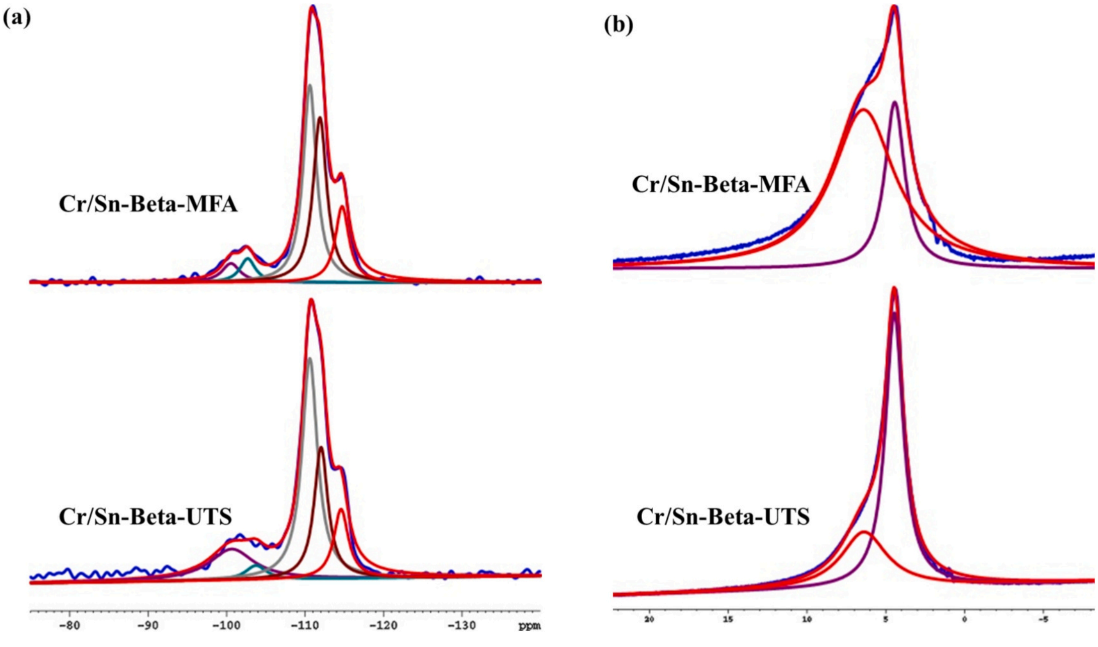

Fig. 4. (a) ^{29}Si MAS NMR and (b) ^{1}H MAS NMR spectra of Cr/Sn-Beta-MFA and Cr/Sn-Beta-UTS.

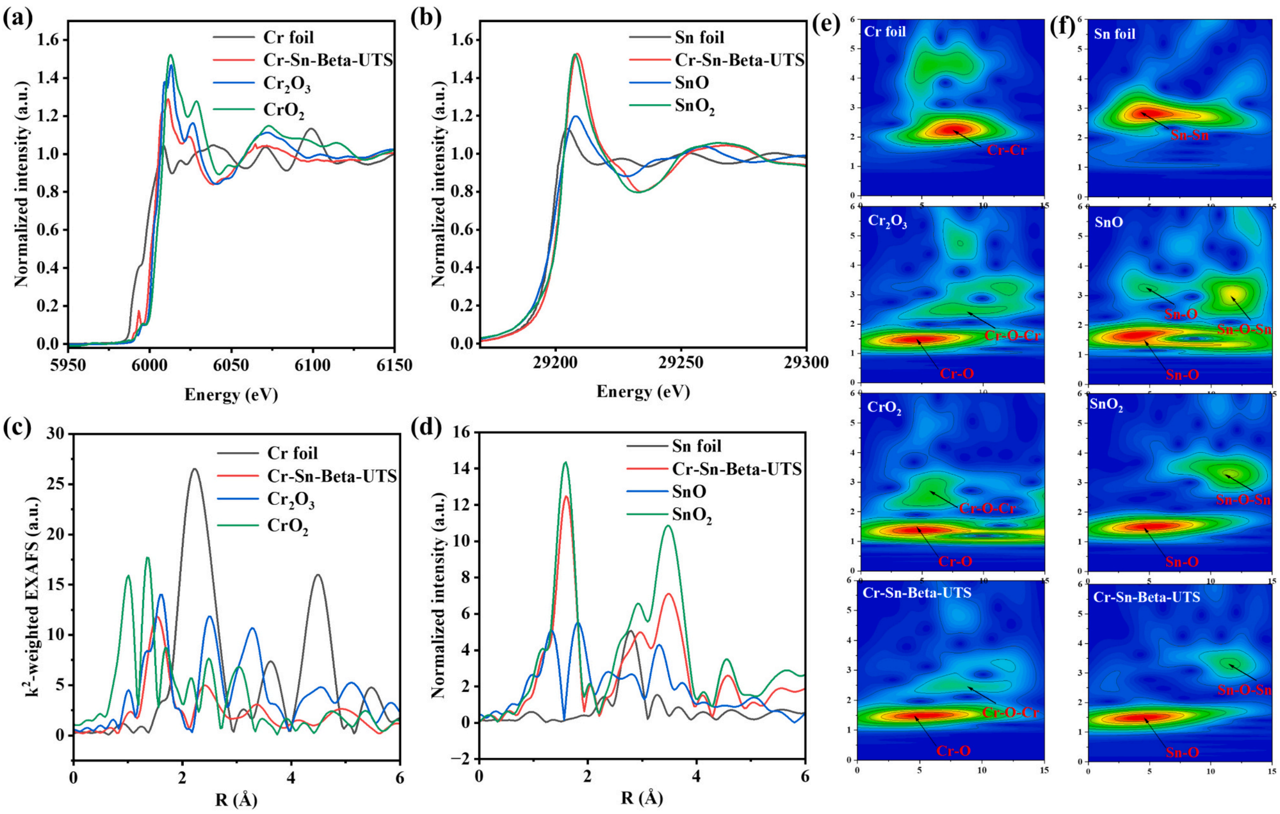

Fig. 5. (a, b) Normalized X-ray absorption near edge structure (XANES) of Cr/Sn-Beta-UTS catalysts; (c, d) radial distance χ(R) spectrogram; (e, f) the wavelet transform spectrogram of Cr/Sn-Beta-UTS. The corresponding references: the Cr foil, Cr_2O_3, CrO_2; the Sn foil, SnO, SnO_2.

contour plots of UTS-treated catalysts showed intense, localized M—O signals and suppressed M—M signals, indicating narrower bond length distributions and superior metal dispersion compared to MFA. These maps also clearly differentiated the spectral features of Cr and Sn from those of metallic foils or bulk oxides (Cr foil, Cr_2O_3, CrO_2; Sn foil, SnO, SnO_2), confirming high-quality dispersion and chemical environment

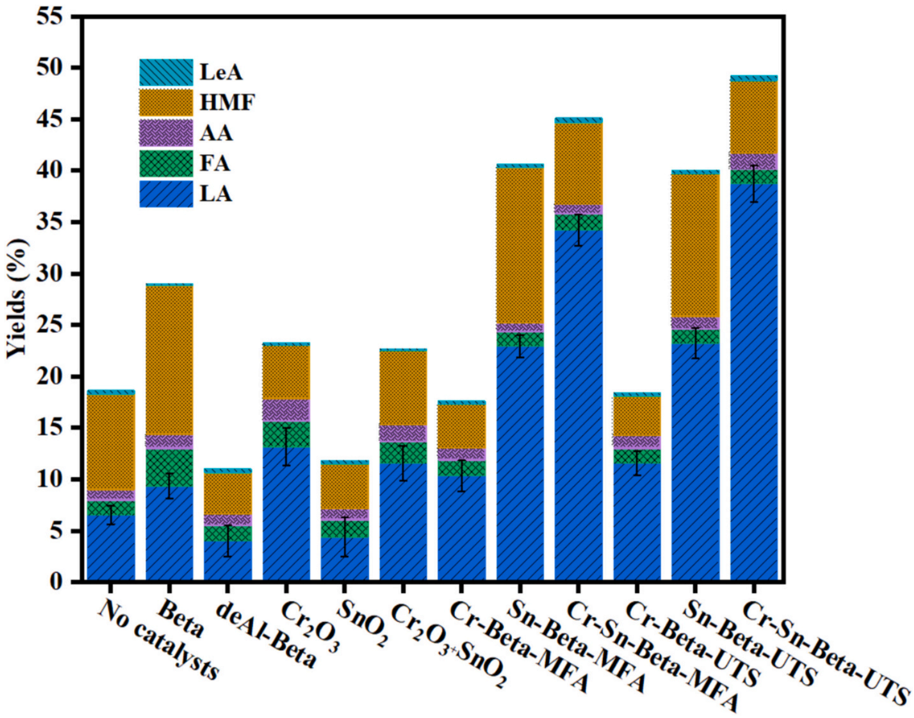

Fig. 6. Blank control experiment for screening catalysts. (Reaction conditions: 230 °C; 2 h; cellulose, 150 mg; catalyst, 150 mg; H_2O, 10 mL) LeA, HMF, AA, FA, LA, denote levulinic acid, hydroxymethylfurfural, acetic acid, formic acid, lactic acid, respectively.

tuning by UTS treatment. The K-space and R-space EXAFS fitting curves are provided in Fig. S5, validating the high-quality fits to the experimental data. Collectively, the combined MAS NMR and XAFS-WT analyses reveal that UTS treatment induces abundant silanol defects, enriches surface acid sites, and promotes the formation of highly dispersed, framework-associated Cr and Sn species, correlating well with the superior catalytic performance in LA production.

3.4. Selective catalytic reaction performance and mechanism analysis

In the research of catalytic reactions, the performance of different catalysts was compared through Fig. 6. Taking the catalyst-free blank group as a reference, it covered Beta zeolite carriers, dealuminated beta, metal oxides, as well as single/double metal loaded catalysts prepared by two methods. The results clearly showed that the performance of bimetallic catalysts exceeded that of single-metal catalysts, and the catalysts prepared by the UTS method outperformed those prepared by the MFA method. In view of this, the subsequent focus is on optimizing the reaction conditions of bimetallic catalysts and analyzing the intermediate products by sampling at different times.

Given the superior LA yield observed for Cr/Sn-Beta-UTS in Fig. 6, we selected this catalyst for further optimization of reaction parameters. As shown in Fig. 7a–d, we systematically studied the effects of Metal dosage, Cr/Sn molar ratio, reaction temperature, and reaction time on LA yield. Under optimized conditions (Metal dosage 0.8 mmol; Cr/Sn = 3:5, 270 °C; 150 mg catalyst, 3 h reaction time), the LA yield reached 52.24%, which is significantly higher than that of other tested conditions. These optimized parameters were thus employed in all subsequent catalytic evaluations. The carbon balance of the catalytic process was evaluated by TOC analysis of both liquid products and solid residues at different reaction times (1 h, 2 h, 3 h, 4 h, and 5 h), as shown in Table S11. The results demonstrated that the carbon recovery ranged from 83.89% to 90.64%, indicating that the majority of the carbon content from cellulose was accounted for and confirming the reliability of the catalytic data.

Reaction conditions: cellulose, 150 mg; catalyst, 150 mg; H_2O, 10 mL; reaction time, 20–180 min. LeA, HMF, AA, FA, LA, Pyru, 1,3-Dihy, Fru, and Glu denote levulinic acid, hydroxymethylfurfural, acetic acid, formic acid, lactic acid, Pyruvaldehyde, 1,3-dihydroxyacetone, fructose and glucose, respectively.

Fig. 8 illustrates the distribution of major intermediates, including levulinic acid (LeA), hydroxymethylfurfural (HMF), acetic acid (AA), formic acid (FA), pyruvaldehyde (Pyru), 1,3-dihydroxyacetone (1,3-Dihy), fructose (Fru), glucose (Glu), and the final product lactic acid (LA) during the conversion of cellulose to LA using Cr/Sn-Beta-MFA and Cr/Sn-Beta-UTS catalysts. In the early stages (20–40 min), glucose and fructose dominate as the primary products, indicating cellulose depolymerization and isomerization into sugar intermediates. As the reaction progresses, especially beyond 60 min, the proportion of LA increases while glucose and fructose decrease, reflecting the further degradation of sugar intermediates into LA. Notably, during the intermediate stage (60–120 min), Cr/Sn-Beta-UTS demonstrates faster LA formation and more focused product distribution, highlighting its superior catalytic activity for intermediate conversion. Throughout the reaction, Cr/Sn-

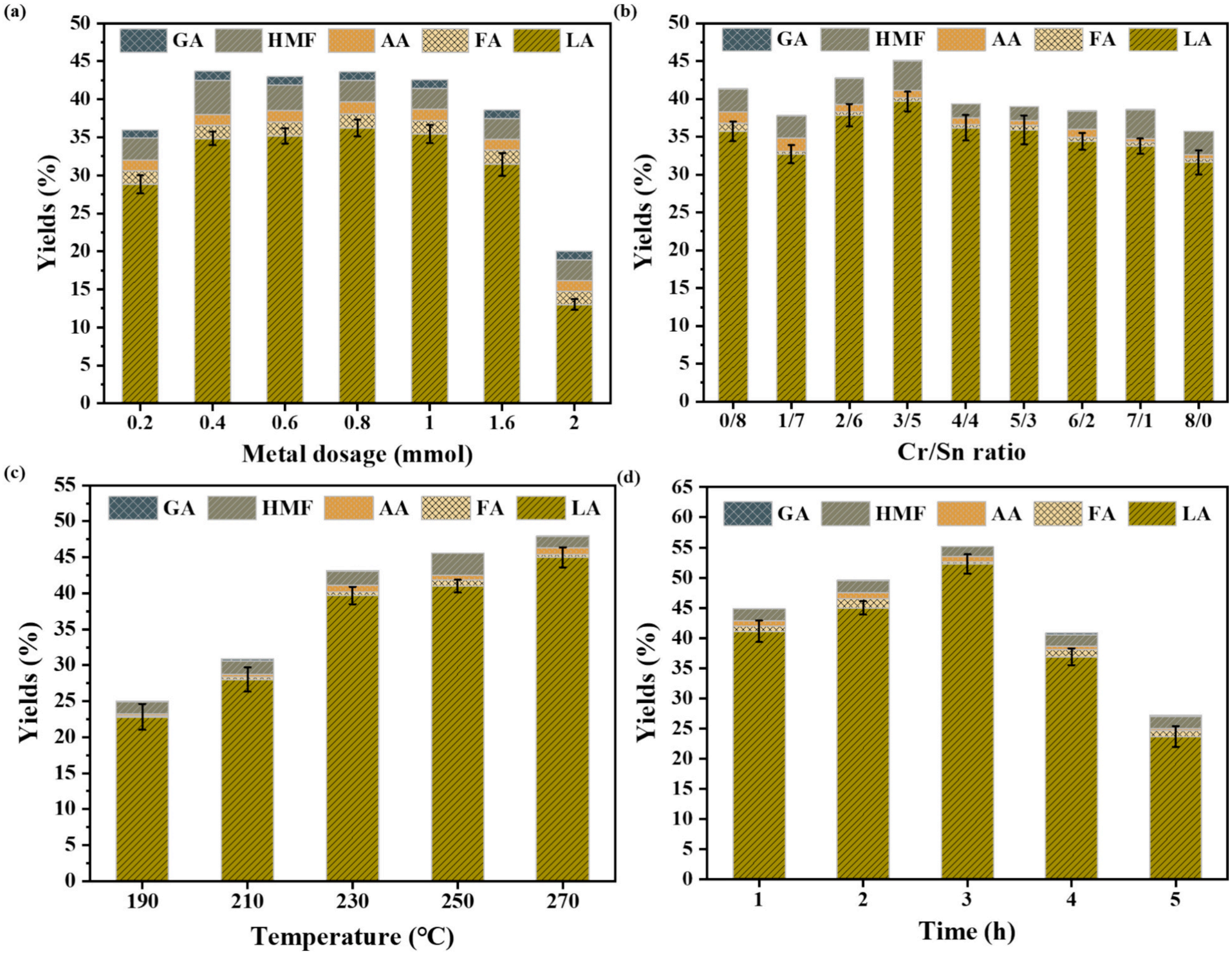

Fig. 7. Optimization of reaction parameters using Cr/Sn-Beta-UTS. (a) Effect of Metal dosage (Cr/Sn = 1:1); (b) Effect of Cr/Sn molar ratio; (c) Effect of reaction temperature (Cr/Sn = 3:5); (d) Effect of reaction time (Cr/Sn = 3:5). (Reaction conditions: cellulose, 150 mg; catalyst, 150 mg; H_2O, 10 mL).

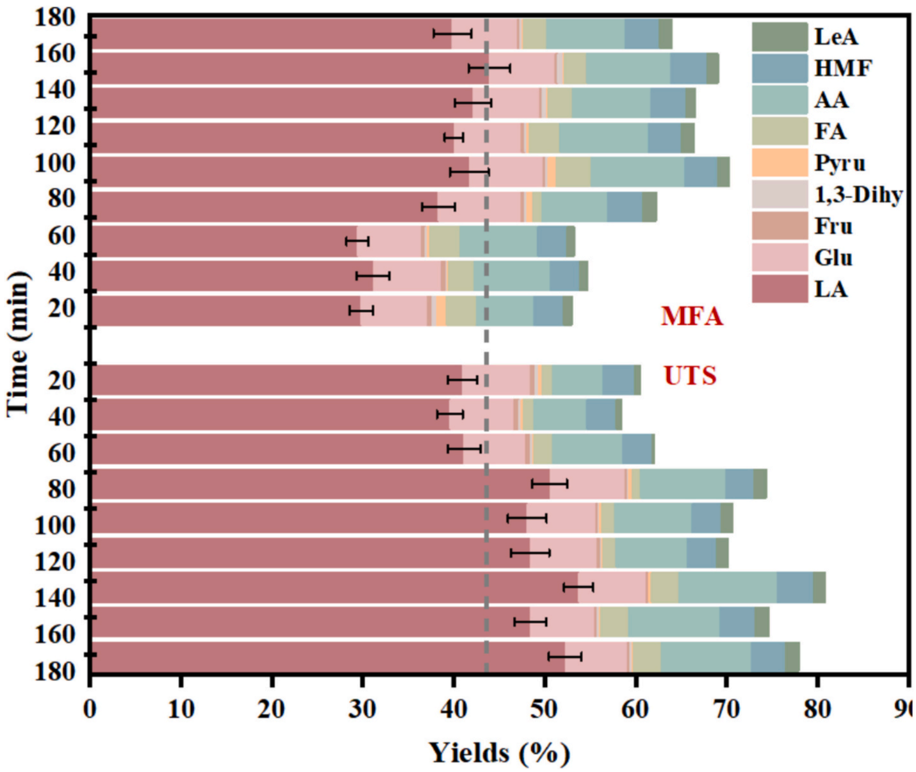

Fig. 8. Catalytic performance of different catalysts for LA and other intermediates conversion.

Beta-UTS achieves higher LA yields with fewer by-products, such as acetic acid and formic acid. In contrast, Cr/Sn-Beta-MFA shows slower LA production and accumulates more unconverted intermediates like fructose and 1,3-dihydroxyacetone, along with increased small-molecule acids. Reportedly, Sn excels in catalyzing carbohydrate isomerization, while Cr is more effective in retro-aldol condensation. These synergistic effects, combined with the higher dispersion of active sites in Cr/Sn-Beta-UTS, account for its enhanced catalytic performance [46]. The synergistic catalytic mechanism between transition metals and tin is governed by the acidic properties of their active sites. Transition metals provide stronger Lewis acid sites, enhancing retro-aldol condensation, while Sn contributes weaker Lewis acid sites, favoring isomerization reactions. The coupling of these two metals effectively tunes the acid site distribution within the zeolite framework. The preparation methods play a pivotal role in constructing catalytic active sites, directly impacting the acid characteristics of the catalysts. These findings underscore that for specific biomass conversion processes, the synergy between particle size effects and acid site distribution in bimetallic catalysts is crucial, significantly influencing their catalytic performance.

Fig. 9a illustrates the detailed reaction pathway for cellulose conversion to LA. The pathway involves several key steps: depolymerization of cellulose into glucose, isomerization of glucose to fructose, further transformation of fructose into intermediates such as 1,3-dihydroxyacetone, and final degradation to form LA. Each step encompasses complex multi-step reactions influenced by the surface acidity and active sites of the catalyst. To elucidate the mechanistic roles of metal sites, C3 intermediates were used as substrates to assess reactivity under different catalysts. As shown in Table S12, Sn-Beta-UTS enabled rapid and selective conversion to LA, while Cr-Beta-UTS exhibited moderate LA yields with higher C3 intermediate interconversion. The bimetallic Cr/Sn-Beta-UTS showed synergistic activity, balancing isomerization and retro-aldol steps to enhance LA production. Fig. 9b presents adsorption energy calculations modeled at the nanoscale for the two catalysts, revealing differences in adsorption energies across various reaction steps. These differences underscore the distinct catalytic behaviors stemming from the structural and surface characteristics of each catalyst

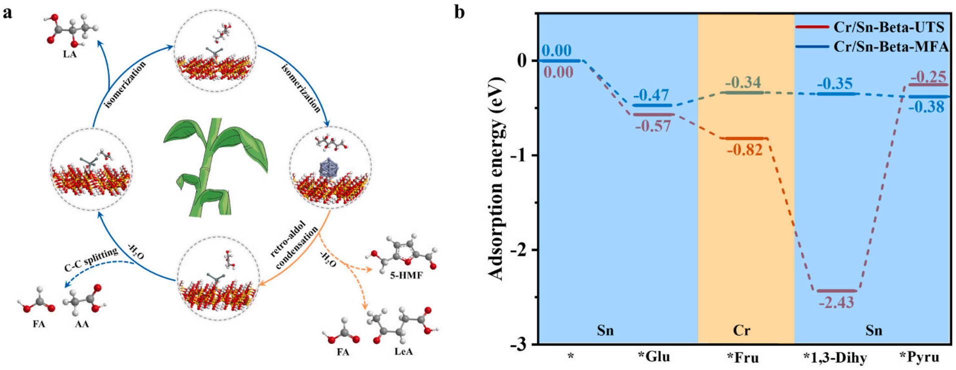

Fig. 9. (a) Reaction network for conversion of cellulose catalyzed by Cr/Sn-Beta-UTS. (b) Adsorption energies screening in cellulose catalysis for Cr/Sn-Beta-UTS and Cr/Sn-Beta-MFA.

[47]. In the critical degradation steps, the adsorption energy for Cr/Sn-Beta-UTS is significantly lower than that for Cr/Sn-Beta-MFA, particularly in two key reactions: the retro-aldol condensation of fructose (adsorption energy of −0.82 eV) and the conversion of the C3 intermediates (−2.43 eV). Lower adsorption energies indicate that Cr/Sn-Beta-UTS exhibits stronger interactions with intermediates, facilitating their stabilization on the catalyst surface and promoting their efficient conversion to LA. In contrast, the higher adsorption energies of Cr/Sn-Beta-MFA lead to shorter residence times of intermediates on the catalyst surface, increasing the likelihood of side reactions and the formation of small-molecule byproducts. This observation aligns with the trends in Fig. 8, where Cr/Sn-Beta-MFA produced more byproducts compared to Cr/Sn-Beta-UTS. Overall, the enhanced performance of Cr/Sn-Beta-UTS is attributed to its optimized surface acidity and metal active sites, which stabilize reaction intermediates and suppress non-selective LA pathways, thereby improving LA yield and selectivity. Conversely, the insufficient intermediate adsorption on Cr/Sn-Beta-MFA results in higher byproduct formation and reduced LA selectivity. To evaluate reusability, Cr/Sn-Beta-UTS was subjected to five consecutive catalytic cycles (Fig. S6, Table S13). The LA yield decreased from 52.24% to 30.11%, while ICP-OES results confirmed gradual leaching of Sn and Cr. Despite this, XRD patterns of fresh and used catalysts (Fig. S7) demonstrated that the Beta framework remained largely intact. These results indicate that the catalyst retains good structural robustness despite partial metal loss. To further validate the applicability of the Cr/Sn-Beta-UTS catalyst beyond cellulose, its catalytic performance toward a series of biomass-derived substrates (e.g., glucose, fructose, xylose, etc.) was evaluated (Table S14). These results confirm the versatility of Cr/Sn-Beta-UTS for various biomass-derived substrates, with LA yields ranging from 28.1% to 67.8%.

4. Conclusion

In this study, an innovative UTS method was developed to successfully prepare Cr-Sn bimetallic nanoparticle catalysts with ultrafine particle size (ca. 2.55 nm), homogeneous dispersion, and high loading capacity, and to investigate the metal particle size effect of non-homogeneous catalysts for specific biomass conversion. Compared with the conventional MFA method, the ultra-high heating/cooling rate and second-short heating duration of the UTS method achieved efficient embedding of Cr and Sn within the zeolite micropores, which conferred precise tailoring of the particle size. Through DFT calculations and mechanistic investigations, we verified that different metals of Cr and Sn acted in different rate-limiting steps by effectively regulating the Lewis acid and Bronsted acid sites, respectively, to effectively improve the LA selectivity and yield, and efficiently inhibit the generation of undesirable by-products during the reaction. Our use of renewable, carbon-neutral biomass and a highly efficient catalyst preparation method with near-100% energy conversion enables an emission-free process, demonstrating the immense potential for sustainable and green production, particularly in reducing energy consumption and avoiding solid waste treatment.

CRediT authorship contribution statement

Mengyu Jin: Writing – original draft, Investigation, Data curation, Formal analysis, Conceptualization, Writing – review & editing. **Yuanbo Song:** Investigation, Conceptualization, Validation. **Shijie Wang:** Conceptualization, Formal analysis. **Cheng Hou:** Investigation, Methodology, Conceptualization. **Xiaoxia Wang:** Investigation. **Yang Shi:** Investigation, Methodology. **Zheng Shen:** Funding acquisition, Writing – review & editing. **Yalei Zhang:** Funding acquisition.

Declaration of competing interest

The authors declare no competing financial interest.

Acknowledgements

This work was supported by the Science and Technology Commission of Shanghai Municipality (Grant No.23DZ1203701 and No.22dz1209302), the International Scientific and Technological Innovation Cooperation Project between the Governments of Key National R&D Program of China (Grant No.2022YFE0120600), the Guizhou Province Science and Technology Project ([2024] Normal 048, [2023] Normal 051, [2024] ZHONGYINDI 023), and the National Natural Science Foundation of China (Grant No.U21A20322).

Appendix A. Supplementary data

Supplementary data to this article can be found online at https://doi.org/10.1016/j.cej.2025.165467.

Data availability

Data will be made available on request.

References

[1] G. Lopez, D. Keiner, M. Fasihi, T. Koiranen, C. Breyer, From fossil to green chemicals: sustainable pathways and new carbon feedstocks for the global chemical industry, Energ. Environ. Sci. 16 (2023) 2879–2909.
[2] J.-Y. Chen, Y. Xiao, F.-S. Guo, K.-M. Li, Y.-B. Huang, Q. Lu, Single-atom metal catalysts for catalytic chemical conversion of biomass to chemicals and fuels, ACS Catal. 14 (2024) 5198–5226.
[3] F. de Clippel, M. Dusselier, R. Van Rompaey, P. Vanelderen, J. Dijkmans, E. Makshina, L. Giebeler, S. Oswald, G.V. Baron, J.F.M. Denayer, P.P. Pescarmona, P.A. Jacobs, B.F. Sels, Fast and selective sugar conversion to alkyl lactate and lactic acid with bifunctional carbon–silica catalysts, J. Am. Chem. Soc. 134 (2012) 10089–10101.
[4] M. Dusselier, P.V. Wouwe, A. Dewaele, E. Makshina, B.F. Sels, Lactic acid as a platform chemical in the biobased economy: the role of chemocatalysis, Energ. Environ. Sci. 6 (2013) 1415–1442.
[5] M. Morales, P.Y. Dapsens, I. Giovinazzo, J. Witte, C. Mondelli, S. Papadokonstantakis, K. Hungerbühler, J. Pérez-Ramírez, Environmental and economic assessment of lactic acid production from glycerol using cascade bio- and chemocatalysis, Energ. Environ. Sci. 8 (2015) 558–567.
[6] F.A. Castillo Martinez, E.M. Balciunas, J.M. Salgado, J.M. Domínguez González, A. Converti, R.P.S. Oliveira, Lactic acid properties, applications and production: a review, Trends Food Sci. Technol. 30 (2013) 70–83.
[7] G. Yan, Y. Tang, Y. Li, Y. Li, L. Nguyen, T. Sakata, K. Higashi, F.F. Tao, P. Sautet, Reaction product-driven restructuring and assisted stabilization of a highly dispersed Rh-on-ceria catalyst, Nat. Catal. 5 (2022) 119–127.
[8] H. Wang, J. Lu, A review on particle size effect in metal-catalyzed heterogeneous reactions, Chin. J. Chem. 38 (2020) 1422–1444.
[9] C.T. Campbell, S.C. Parker, D.E. Starr, The effect of size-dependent nanoparticle energetics on catalyst sintering, Science 298 (2002) 811–814.
[10] J. Xue, Y. Wang, Y. Meng, X. Zhou, G. Pan, S. Xia, Theoretical investigation of decarbonylation mechanism of furfural on Pd(111) and M/Pd(111)(M = Ru, Ni, Ir) surfaces, Mol. Catal. 493 (2020) 111054.
[11] S. Xia, L. Fang, Y. Meng, X. Zhang, L. Zhang, C. Yang, Z. Ni, Water-gas shift reaction catalyzed by layered double hydroxides supported Au-Ni/Cu/Pt bimetallic alloys, Appl. Catal. Environ. 272 (2020) 118949.
[12] H. Sharma, A. Dhir, Hydrogen augmentation of biogas through dry reforming over bimetallic nickel-cobalt catalysts supported on titania, Fuel 279 (2020) 118389.
[13] B.Y. Park, Y.J. Kim, M.S. Han, In situ generated bimetallic nanoparticle catalysts for the transfer semihydrogenation of azoarenes, ACS Sustain. Chem. Eng. 12 (2024) 11274–11282.
[14] L. Liu, A. Corma, Bimetallic sites for catalysis: from binuclear metal sites to bimetallic nanoclusters and nanoparticles, Chem. Rev. 123 (2023) 4855–4933.
[15] T. Miyake, T. Asakawa, Recently developed catalytic processes with bimetallic catalysts, Appl. Catal. Gen. 280 (2005) 47–53.
[16] J.H. Sinfelt, Catalysis by alloys and bimetallic clusters, Acc. Chem. Res. 10 (1977) 15–20.
[17] X. Zhao, G. Wu, X. Zheng, P. Jiang, J. Yi, H. Zhou, X. Gao, Z.-Q. Yu, Y. Wu, A double atomic-tuned RuBi SAA/Bi@OG nanostructure with optimum charge redistribution for efficient hydrogen evolution, Angew. Chem. Int. Ed. 62 (2023) e202300879.
[18] Z. Zhao, J. Sun, X. Li, S. Qin, C. Li, Z. Zhang, Z. Li, X. Meng, Engineering active and robust alloy-based electrocatalyst by rapid Joule-heating toward ampere-level hydrogen evolution, Nat. Commun. 15 (2024) 7475.
[19] X. Liu, X. Cai, Y. Zhu, Catalysis synergism by atomically precise bimetallic nanoclusters doped with heteroatoms, Acc. Chem. Res. 56 (2023) 1528–1538.
[20] Q. Shi, Z. Qin, S. Sharma, G. Li, Recent progress in heterogeneous catalysis by atomically and structurally precise metal nanoclusters, Chem. Rec. 21 (2021) 879–892.

[21] R. Ferrando, J. Jellinek, R.L. Johnston, Nanoalloys: from theory to applications of alloy clusters and nanoparticles, Chem. Rev. 108 (2008) 845–910.

[22] A. Corma, P. Concepción, M. Boronat, M.J. Sabater, J. Navas, M.J. Yacaman, E. Larios, A. Posadas, M. López-Quintela, D. Buceta, E. Mendoza, G. Guilera, A. Mayoral, Exceptional oxidation activity with size-controlled supported gold clusters of low atomicity, Nat. Chem. 5 (2013) 775–781.

[23] W. Zhang, X. Wei, T. Wu, F. Wei, L. Ma, Y. Lv, W. Zhou, H. Liu, Carbothermal shock enabled functional nanomaterials for energy-related applications, Nano Energy 118 (2023) 108994.

[24] T. Risse, S. Shaikhutdinov, N. Nilius, M. Sterrer, H.-J. Freund, Gold supported on thin oxide films: from single atoms to nanoparticles, Acc. Chem. Res. 41 (2008) 949–956.

[25] T.W. Hansen, A.T. DeLaRiva, S.R. Challa, A.K. Datye, Sintering of catalytic nanoparticles: particle migration or Ostwald ripening? Acc. Chem. Res. 46 (2013) 1720–1730.

[26] Y. Yao, Z. Huang, P. Xie, L. Wu, L. Ma, T. Li, Z. Pang, M. Jiao, Z. Liang, J. Gao, Y. He, D.J. Kline, M.R. Zachariah, C. Wang, J. Lu, T. Wu, T. Li, C. Wang, R. Shahbazian-Yassar, L. Hu, High temperature shockwave stabilized single atoms, Nat. Nanotechnol. 14 (2019) 851–857.

[27] R. Jiang, Y. Da, X. Han, Y. Chen, Y. Deng, W. Hu, Ultrafast synthesis for functional nanomaterials, Cell Rep. Phys. Sci. 2 (2021) 100302.

[28] L. Zhu, Z. Lai, J. Xu, P. Ma, J. Lu, Q. Xu, Y. Lin, L. Zheng, L. Wu, H. Ding, J. Ge, Y. Ye, Ultrafast flash Joule heating synthesis of the Pt/MoOx heterostructure for enhancing the electrocatalytic hydrogen evolution reaction, J. Mater. Chem. A 12 (2024) 28149–28160.

[29] Y. Chen, G.C. Egan, J. Wan, S. Zhu, R.J. Jacob, W. Zhou, J. Dai, Y. Wang, V. A. Danner, Y. Yao, K. Fu, Y. Wang, W. Bao, T. Li, M.R. Zachariah, L. Hu, Ultra-fast self-assembly and stabilization of reactive nanoparticles in reduced graphene oxide films, Nat. Commun. 7 (2016) 12332.

[30] M. Cui, C. Yang, S. Hwang, B. Li, Q. Dong, M. Wu, H. Xie, X. Wang, G. Wang, L. Hu, Rapid atomic ordering transformation toward intermetallic nanoparticles, Nano Lett. 22 (2022) 255–262.

[31] X. Wang, Z. Huang, Y. Yao, H. Qiao, G. Zhong, Y. Pei, C. Zheng, D. Kline, Q. Xia, Z. Lin, J. Dai, M.R. Zachariah, B. Yang, R. Shahbazian-Yassar, L. Hu, Continuous 2000 K droplet-to-particle synthesis, Mater. Today 35 (2020) 106–114.

[32] Y. Qiao, S. Xu, Y. Liu, J. Dai, H. Xie, Y. Yao, X. Mu, C. Chen, D.J. Kline, E.M. Hitz, B. Liu, J. Song, P. He, M.R. Zachariah, L. Hu, Transient, in situ synthesis of ultrafine ruthenium nanoparticles for a high-rate Li–CO2 battery, Energ. Environ. Sci. 12 (2019) 1100–1107.

[33] X. Hou, X. Yu, M. Liu, H. Peng, L. Wu, L. Liao, G. Lv, Ultrafast synthesis of Mo2N with highly dispersed Ru for efficient alkaline hydrogen evolution, Chin. Chem. Lett. 36 (2025) 109845.

[34] W. Shi, Z. Li, Z. Gong, Z. Liang, H. Liu, Y.-C. Han, H. Niu, B. Song, X. Chi, J. Zhou, H. Wang, B.Y. Xia, Y. Yao, Z.-Q. Tian, Transient and general synthesis of high-density and ultrasmall nanoparticles on two-dimensional porous carbon via coordinated carbothermal shock, Nat. Commun. 14 (2023) 2294.

[35] J. Zhang, S. Bo, W. Liao, K. Yang, T. Su, H. Lü, Z. Zhu, Zeolitic framework Sn boosts the 2,5-dimethylfuran selectivity for the hydrodeoxygenation of 5-hydroxymethylfurfural over Co/Sn-Beta catalyst, Chem. Eng. J. 484 (2024) 149511.

[36] A. Śrębowata, R. Baran, S. Casale, I.I. Kamińska, D. Łomot, D. Lisovytskiy, S. Dzwigaj, Catalytic conversion of 1,2-dichloroethane over bimetallic Cu–Ni loaded BEA zeolites, Appl. Catal. Environ. 152-153 (2014) 317–327.

[37] B. Tang, W. Dai, X. Sun, G. Wu, L. Li, N. Guan, M. Hunger, Incorporation of cerium atoms into Al-free Beta zeolite framework for catalytic application, Chin. J. Catal. 36 (2015) 801–805.

[38] J. Janas, J. Gurgul, R.P. Socha, T. Shishido, M. Che, S. Dzwigaj, Selective catalytic reduction of NO by ethanol: speciation of iron and “structure–properties” relationship in FeSiBEA zeolite, Appl. Catal. Environ. 91 (2009) 113–122.

[39] S. Dzwigaj, L. Stievano, F.E. Wagner, M. Che, Effect of preparation and metal content on the introduction of Fe in BEA zeolite, studied by DR UV–Vis, EPR and Mössbauer spectroscopy, J. Phys. Chem. Solid 68 (2007) 1885–1891.

[40] J. Dijkmans, J. Demol, K. Houthoofd, S. Huang, Y. Pontikes, B. Sels, Post-synthesis Snβ: an exploration of synthesis parameters and catalysis, J. Catal. 330 (2015) 545–557.

[41] E. Peeters, G. Pomalaza, I. Khalil, A. Detaille, D.P. Debecker, A.P. Douvalis, M. Dusselier, B.F. Sels, Highly dispersed Sn-Beta zeolites as active catalysts for Baeyer–Villiger oxidation: the role of mobile, in situ Sn(II)O species in solid-state stannation, ACS Catal. 11 (2021) 5984–5998.

[42] M. Lezanska, G.S. Szymanski, P. Pietrzyk, Z. Sojka, J.A. Lercher, Characterization of Cr−MCM-41 and Al,Cr−MCM-41 mesoporous catalysts for gas-phase oxidative dehydrogenation of cyclohexane, J. Phys. Chem. C 111 (2007) 1830–1839.

[43] Y. Wang, Z.-P. Hu, W. Tian, L. Gao, Z. Wang, Z.-Y. Yuan, Framework-confined Sn in Si-Beta stabilizing ultra-small Pt nanoclusters as direct propane dehydrogenation catalysts with high selectivity and stability, Catal, Sci. Technol. 9 (2019) 6993–7002.

[44] Z. Ai, Y. Cheng, L. Zhang, J. Qiu, Efficient removal of Cr(VI) from aqueous solution with Fe@Fe2O3 core−shell nanowires, Environ. Sci. Technol. 42 (2008) 6955–6960.

[45] Z. Xu, Y. Yue, X. Bao, Z. Xie, H. Zhu, Propane dehydrogenation over Pt clusters localized at the Sn single-site in zeolite framework, ACS Catal. 10 (2020) 818–828.

[46] M. Xia, Z. Shen, S. Xiao, B. Peng, M. Gu, W. Dong, Y. Zhang, Synergistic effects and kinetic evidence of a transition metal-tin modified Beta zeolite on conversion of Miscanthus to lactic acid, Appl. Catal. Gen. 583 (2019) 117126.

[47] Y. Wang, C. Wang, L. Wang, L. Wang, F.-S. Xiao, Zeolite fixed metal nanoparticles: new perspective in catalysis, Acc. Chem. Res. 54 (2021) 2579–2590.